

Chapter 7

Spectra

In this chapter, the basic principles of spectrograph design and the reduction of the spectra into science ready form are reviewed. Derivations of the optical principles are not given, but only results that are central to a basic understanding of the dispersion relations, the spectral purity, and the resolution of the spectra. Though dispersion of the light can be obtained via prisms or gratings, only the properties of gratings are discussed (since they are most common).

Also discussed are the resolving power, pixel sample rate, and the so-called “resolution element”. Extraction of the data into a science-ready state first involves several calibration steps, which is performed on the raw data (a two dimensional illumination profile) using a suite of calibration data. The uncertainties in the extracted spectrum provide the signal-to-noise ratio at each wavelength, for which the treatment is discussed in some detail. Also addressed are flux calibration, a robust method for continuum estimation, and a treatment for combining several spectra of the same object.

7.1 The Spectrograph

The basic components of a spectrograph are the entrance slit, a collimator, a grating or prism, a camera, and the detector. It is common for the dispersive element in modern spectrographs to be a grating. As shown in Fig. 7.1, the light first enters the slit. The slit (1) is located at the focal point of the telescope and the light beam is diverging as the light path exits the slit. The light is then collimated by the collimator (2), which is located at a distance f_{coll} from the slit. The collimated light then strikes

the disperser, which is a ruled grating (3). The grating is tilted with respect to the incoming light path. The reflected light is then focused by a camera (4) with focal length f_{cam} onto the detector (5).

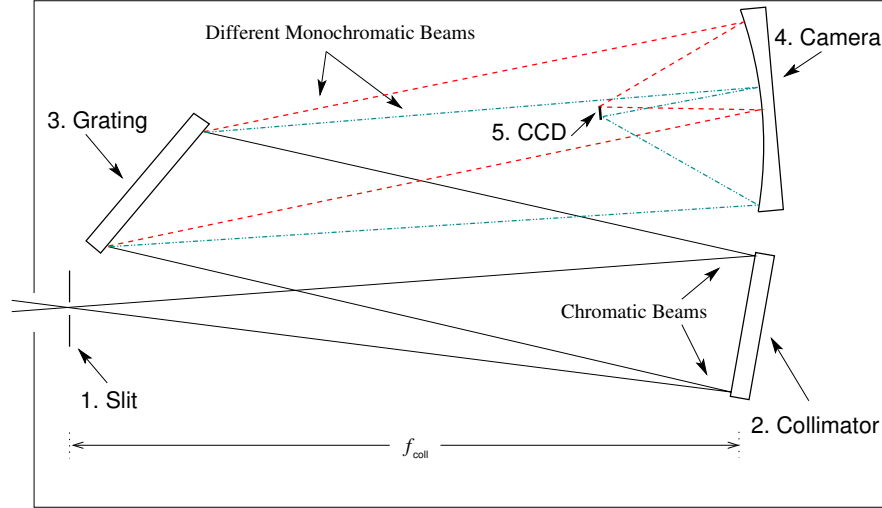


Figure 7.1: — A schematic of a grating spectrograph showing the optical layout and light path from slit to detector. The distance from the collimator is the collimator focal length, f_{coll} , and the distance from the camera mirror to the detector is f_{cam} . The light is focused by the telescope on the plane of the slit. The chromatic beam (solid lines) then diverges until it is parallelized by the collimator. After the light reflects off the grating, the light is organized into monochromatic beams with different wavelengths (dash-dash and dash-dot lines) due to diffraction; each monochromatic beam propagates in a unique direction. These beams are then focused by the camera at different spatial locations along the detector, forming the spectrum.

Modern detectors are usually charged coupled devices, or CCDs, with finite pixels, which results in a discretized sampling of the dispersed light. The illumination profile of the spectrum has a dispersion direction and a spatial direction. The magnification of the spatial direction along the slit on the detector is given by f_{cam}/f_{coll} . The dispersion direction will have a spectral purity, $\Delta\lambda$, governed by the spectrograph design, primarily by the width of the slit, w , the collimator focal length, f_{coll} , the distance between grating lines, d , the spectral order, n , and the grating angle of incidence, α (see § 7.1.5). There are secondary effects governing the shape of the illumination profile and the spectral purity, such as the stability of the image of the source on the slit (tracking), the atmospheric seeing, and the angle of the slit with respect to the parallactic angle (perpendicular to the horizon).

7.1.1 Diffraction Gratings

A typical grating can be characterized by equally spaced grooves, called facets. Consider a grating of length L , as illustrated in Fig 7.2, with facet widths s and with center-to-center spacings d , with the condition $d > s$. The ratio L/d gives the number of facets, N_f , on the grating. It is important to keep in mind that for the following discussion, all relations apply to a monochromatic diffracted light beam (even though the incoming light is chromatic). The full response behavior of a spectrograph is obtained by considering the combined behavior of the diffracted monochromatic beams over the wavelength range of the incoming chromatic beam.

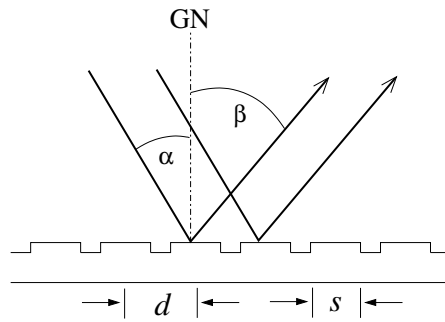


Figure 7.2: A schematic of a reflection grating showing the individual grooves, or facets. The facets are characterized by their edge-to-edge lengths, s , and center-to-center separation d . The incoming light has an angle of incidence α , measured with respect to the grating normal, GN. Interference of the reflected wave fronts yields a diffraction angle, β , which is a function of wavelength phase differences (Eq. 7.1).

For a specific spectrograph design, the grating is tilted so that the angle of incidence of the incoming collimated chromatic light is α with respect to the grating normal. After interaction with the grating, the light is diffracted at wavelength dependent angles, β ; there is a unique value of β for each wavelength, λ , that depends upon wavelength phase differences. For reflection gratings, as shown in Fig. 7.2, β is defined to be negative.

As discussed in the following sections, there are two interference patterns that govern the angular dependence of the intensity function (fraction of transmitted intensity) at each wavelength. The first is due to phase differences between the centers of adjacent facets, φ_{cc} . The second is due to phase differences between the center and edge of each facet, φ_{ce} . Further details on diffraction gratings and the principles of diffraction gratings can be found in Hecht & Zajac (1974), Shroeder (1987), and Gray (1992).

7.1.1.1 The Grating Equation

Light with wavelength λ is “reflected” at an angle of diffraction that corresponds to constructive interference, or facet center to facet center phase differences of $\varphi_{cc} = n\pi$. The relationship between the diffraction angle and the wavelength is given by the grating equation,

$$\frac{n\lambda}{d} = \sin \alpha + \sin \beta, \quad (7.1)$$

where the integer n is called the diffraction order. The angular dispersion with wavelength is obtained by differentiating Eq. 7.1,

$$\frac{d\beta}{d\lambda} = \frac{n}{d \cos \beta} = \frac{\sin \alpha + \sin \beta}{\lambda \cos \beta}, \quad (7.2)$$

from which it is clear that the angular dispersion increases with larger n and smaller d .

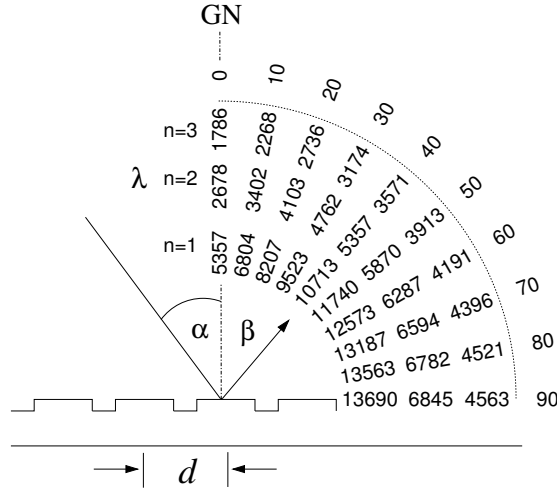


Figure 7.3: A schematic of the behavior of a grating with $1/d = 1200$ facets mm^{-1} for an incident angle $\alpha = 40^\circ$. At each diffraction angle, β , the wavelengths for orders $n = 1, 2$, and 3 are tabulated, as governed by equation (Eq. 7.1). For $n = 0$, there is no dispersion and chromatic light beam is diffracted at $\beta = -\alpha$. Phase differences in the light reflection off adjacent facets interfere constructively for $\varphi_{cc} = n\pi$ for each λ , which yields monochromatic beams each diffracted at a unique β . Note that the dispersion increases with n according to Eq. 7.2.

The behavior of the grating equation (Eq. 7.1) is illustrated in Fig. 7.3, for orders $n = 1, 2$, and 3 for a grating with $1/d = 1200$ facets mm^{-1} for an incident angle $\alpha = 40^\circ$. For $n = 0$, there is no dispersion and all

wavelengths of the chromatic incident beam are diffracted at angle $\beta = -\alpha$. As n increases, the dispersion increases. For the example grating, if one wished to observe a wavelengths in the regime of 6000 Å, the camera would need to be placed at $\beta = 5^\circ$ for $n = 1$ (lowest) dispersion or $\beta = 55^\circ$ for $n = 2$ (higher) dispersion.

7.1.1.2 Free Spectral Range

As can be seen in Fig. 7.3, the camera can be placed to capture the spectrum for any desired order. However, there are multiple $n\lambda$ that satisfy Eq. 7.1 for a given β . Thus, there are wavelengths in recursive orders that are diffracted into the same direction. This results in spatial overlap of wavelengths satisfying $(n-1)\lambda_{n-1} = n\lambda_n$, which is obtained by the ratio of the grating equation for adjacent orders.

The free spectral range for order n is defined as the wavelength range,

$$\Delta\lambda_n^+ = \lambda_{n-1} - \lambda_n, \quad (7.3)$$

$$\Delta\lambda_n^- = \lambda_n - \lambda_{n+1}, \quad (7.4)$$

for a given β . After substitution of the recursive relationship, $(n-1)\lambda_{n-1} = n\lambda_n$, we have

$$\Delta\lambda_n^+ = \lambda_n/(n-1), \quad (7.5)$$

$$\Delta\lambda_n^- = \lambda_n/(n+1). \quad (7.6)$$

Consider the free spectral range for the example grating illustrated in Fig 7.3 for $\beta = 40^\circ$ at $n = 2$, which diffracts wavelength 5357 Å. We have $\Delta\lambda_2^+ = 5357/(2-1) = 5357$ Å, which yields 10713 Å for $\beta = 40^\circ$ at $n = 1$, and $\Delta\lambda_2^- = 5357/(2+1) = 1786$ Å, which yields 3571 Å for $\beta = 40^\circ$ at $n = 3$. Examination of Fig 7.3 illustrates this case.

The spatial overlap of different wavelengths can cause confusion in the recorded spectrum. There are two solutions to mitigate this confusion, depending upon whether the spectrograph is designed for low order or high order diffraction. In the case of small n , a blocking filter is placed in the light path (before the dispersion grating will work). For large n , a cross-dispersing grating is placed in the light path, after the dispersion grating. This latter approach is used for echelle spectrographs.

7.1.1.3 The Interference Function

In reality, there is a continuum of center-center interference phases that are periodic over continuous multiples of π . The generalized relationship

between φ_{cc} , β , and each monochromatic diffracted λ is governed by

$$\varphi_{cc} = \frac{\pi d}{\lambda} (\sin \alpha + \sin \beta). \quad (7.7)$$

Substituting $\varphi_{cc} = n\pi$ into Eq 7.7, yields the grating equation (Eq. 7.1). The pattern of the normalized intensity for λ is called the interference function and is given by

$$I_i(\varphi_{cc}) = \frac{\sin^2(L/d)\varphi_{cc}}{\sin^2 \varphi_{cc}}, \quad (7.8)$$

where $L/d = N_f$, is an integer. For a given λ , there is a range of interference phases, which yield maximum intensity for $\varphi_{cc} = n\pi$ (constructive interference) and zero intensity for $\varphi_{cc} = (n/2)\pi$ (destructive interference).

In Fig. 7.4, the intensity function (Eq. 7.8) is plotted as a function of φ_{cc} for fixed λ . It is clear that the intensity pattern recorded for a given λ is not a δ -function, but is “smeared” over a small range of phase differences $\Delta\varphi_{cc} = \lambda/N_f d = \lambda/L$. The order separation of the peaks occurs when φ_{cc} is an integer multiple of λ/d .

Consider the example grating illustrated in Fig 7.3. For $\lambda = 5357 \text{ \AA}$ in first order ($n = 1$), the diffraction angle is $\beta = 0^\circ$, and for $n = 2$ is $\beta = 40^\circ$. Naively, it would appear that one could place the camera at either location depending upon the desired dispersion (higher n location for higher disperion). However, as we will see below, the resulting intensity of the diffracted light is not equal for all orders for this type of grating due to additional phase differences introduced by the facet sizes, s .

7.1.1.4 The Blaze Function

As described by Eq. 7.8 and as illustrated in Fig. 7.4, the intensity pattern due to center-center diffraction is periodic and symmetric for all n . However, there is additional phase modulations that occur due to interference phases between the center and the edge of each facet. For center-edge interference, the relationship between β , λ , and the the center-edge phase φ_{ce} is

$$\varphi_{ce} = \frac{\pi s}{\lambda} (\sin \alpha + \sin \beta). \quad (7.9)$$

The pattern of the normalized intensity for this inteference, called the blaze function, is given by

$$I_b(\varphi_{ce}) = \frac{\sin^2 \varphi_{ce}}{\varphi_{ce}^2}. \quad (7.10)$$

The blaze function is a maximum when $\varphi_{ce} = 0$, which occurs when the incident and diffraction angle are symmetric about the facet (grating)

normal, i.e., $\alpha = -\beta$. For plane-parallel (untilted) facets, as shown in Fig. 7.3, this condition is met for $n = 0$ only. The minima occur at $\varphi_{ce} = n\pi$, so that the phase difference spread of the blaze function is $\Delta\varphi_{ce} = \lambda/s$. Note that this is a significantly broader width than that of the interference function, $\Delta\varphi_{cc} = \lambda/L$.

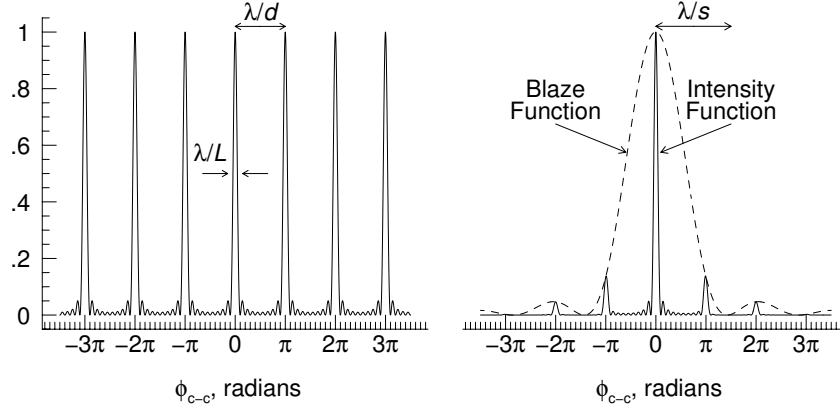


Figure 7.4: (left) The periodic interference function, Eq. 7.8, which results from the facet center-to-center interference, plotted as a function of the phase difference (in units of π) for an arbitrary wavelength λ . Note the peaks are at $n\pi$, where n is an integer. For this example, $N_f = L/d = 10$, which is an unrealistic configuration used here only for illustration purposes. A typical grating might have $L = 40$ cm with 600 facets mm^{-1} , which gives $N_f = L/d = 24,000$; thus, real gratings have much narrower $\Delta\varphi_{cc}$ peaks. Note that each peak satisfies the grating equation (Eq. 7.1) and is thus diffracted at different β . — (right) The blaze function, Eq. 7.10, which results from facet center-to-edge interference also plotted as a function of the phase difference of the center-center diffraction. The width of the blaze function is governed by the facet sizes; for this example the ratio $s/d = 0.7$ was used. The blaze function modulates the interference function, giving the overall intensity pattern, Eq. 7.12.

Naively, it might appear that φ_{ce} is a periodic function and that Eq. 7.10 would have multiple maxima, but this is not the case. The behavior of the blaze function for a given wavelength at various orders is more clearly seen by solving the grating equation (Eq. 7.1) for λ and substituting into Eq. 7.9, which yields

$$I_b(n) = \frac{\sin^2 n\pi(s/d)}{[n\pi(s/d)]^2}, \quad (7.11)$$

the relative blaze intensity for order n . It is because $d \neq s$ that φ_{ce} , and thus $I_b(n)$, is not periodic. Note that $I_b(n)$ peaks at $n = 0$ and decreases as n^2 . The interpretation is that for a given λ appearing in multiple orders, the relative intensity is governed by Eq. 7.11.

It is not desirable to have the blaze function peak at $n = 0$, where there

is no dispersion. The remedy is to “blaze” the grating by tilting the facets, which shifts the blaze peak. As we will show, it also yields blaze peaks for all values of n . This is discussed in § 7.1.1.6.

7.1.1.5 The Intensity Function

The resulting intensity function for light of wavelength λ , is the product of the interference and blaze functions,

$$I(\lambda) = I_i(\varphi_{cc}) \cdot I_b(\varphi_{ce}) = \frac{\sin^2(L/d)\varphi_{cc}}{\sin^2 \varphi_{cc}} \cdot \frac{\sin^2 \varphi_{ce}}{\varphi_{ce}^2}. \quad (7.12)$$

As shown in Fig. 7.4, the resulting intensity pattern is simply the interference function modulated by the blaze function. Note that, for a non-blazed grating, the peak of the intensity occurs at $n = 0$, when $\alpha = -\beta$ (see Fig. 7.3) and the interference due to center-edge phase differences significantly reduces the throughput of light at higher orders. Again, this is more clearly seen by solving the grating equation (Eq. 7.1) for λ and substituting into Eq. 7.12, which yields the relative intensity for order n ,

$$I(n) = I_i(n) \cdot I_b(n) = \frac{\sin^2 n\pi(s/d)}{[n\pi(s/d)]^2}, \quad (7.13)$$

where $I_i(n) = 1$ for all n . Thus, the relative intensity of a given wavelength at order n is modulated strictly by the blaze function.

Again, consider the example grating shown in Fig. 7.3 for the ratio $s/d = 0.7$. To observe wavelength 5357 Å with the lowest dispersion ($n = 1$ and $\beta = 0^\circ$) would be less than ideal because the intensity is modulated to roughly 10% its $n = 0$ throughput. Observing this wavelength at higher dispersion ($n = 2$ and $\beta = 40^\circ$), would pose an even greater challenge because the intensity is modulated down even further. Note that 5357 Å does not appear in order $n = 3$ and above. By decreasing the ratio s/d , the blaze function can be broadened so that the throughput is increased for $n > 0$. However, this is not the most effective solution.

7.1.1.6 Blazing a Grating

As shown above, the maximum efficiency in the intensity function occurs when the incident, α , and diffraction, β , angles are symmetric about the facet normal, which is the same as the grating normal, GN, when the grating facets are not tilted (as shown in the example grating in Figs. 7.2 and 7.3).

From Eq. 7.2, we see that the dispersion, $d\beta/d\lambda$, scales as d/n , so in order to obtain a given resolving power for a spectrograph, it is desirable to

maximize the intensity function (Eq. 7.12) for the required d and n combination. However, unless the blaze function is modified in some manner, the intensity pattern is maximized for $n = 0$ (no dispersion!) and is significantly reduced for large n .

In order to maximize the throughput at higher orders, the peak of the blaze function must be “shifted” along the φ_{ce} axis in Fig. 7.4 such that it is centered at the desired n . By tilting the grating facets by an angle ϕ , as shown in Fig. 7.5, the center-edge diffraction pattern can be phase shifted. In fact, blazing the grating has the added effect that the blaze function has a peak for all n when the incident and diffraction angles are symmetric about the facet normal (which occurs for different λ for each n).

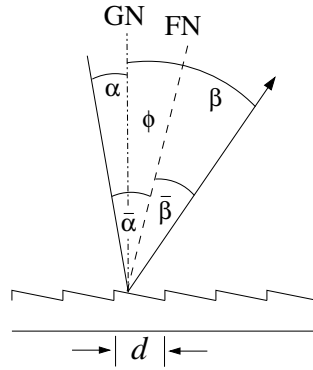


Figure 7.5: To maximize the diffraction illumination pattern for $n > 0$, a phase shift is introduced to the center-edge diffraction interference by grooving the facets at an angle ϕ , which also defines the facet normal, FN. The blaze function then peaks when $\bar{\beta} = -\bar{\alpha}$.

The configuration for a blazed grating with facet tilts, ϕ , is illustrated in Fig. 7.5. The facet lengths are now $s = d \cos^2 \phi$, and the center-edge diffraction is based upon the angles with respect to the facet normal (FN, as is the case for the special case $\phi = 0^\circ$). Defining the incident angle with respect to FN as $\bar{\alpha} = \alpha - \phi$ and the diffraction angle $\bar{\beta} = \beta - \phi$ (ϕ , α , and $\bar{\alpha}$ are defined positive, whereas β and $\bar{\beta}$ are negative), Eq. 7.9 is rewritten,

$$\varphi_{ce} = \frac{\pi s}{\lambda} [\sin \bar{\alpha} + \sin \bar{\beta}], \quad (7.14)$$

$$= \frac{\pi d \cos^2 \phi}{\lambda} [\sin(\alpha - \phi) + \sin(\beta - \phi)]. \quad (7.15)$$

Recall that the blaze function (Eq. 7.10) is a maximum when $\varphi_{ce} = 0$. Thus, the optimal relationship between the facet tilts and the angles of incident and diffraction with respect to the grating normal, GN, is obtained when

$\alpha - \phi = -(\beta - \phi)$, or $\phi = (\alpha + \beta)/2$. We will show that the blaze function for tilted facets peaks for all n at the λ dispersed into the $\bar{\beta} = -\bar{\alpha}$ direction, which occurs when the incident and diffraction angles are symmetric about the facet normal.

The wavelength at which the blaze function peaks at each order can be computed from the grating equation (Eq. 7.1). We have

$$\frac{n\lambda}{d} = \sin \alpha + \sin \beta, \quad (7.16)$$

$$= \sin(\bar{\alpha} + \phi) + \sin(\bar{\beta} + \phi). \quad (7.17)$$

Applying $\bar{\beta} = -\bar{\alpha}$, where the blaze function maximizes, yields,

$$\frac{n\lambda_b}{d} = 2 \sin \phi \cos \bar{\alpha} = 2 \sin \phi \cos(\alpha - \phi), \quad (7.18)$$

where λ_b is called the blaze wavelength for order n .

The general behavior of a blazed grating is more clearly seen by solving for d/λ_b in Eq. 7.18 and substituting into Eq. 7.14, which yields

$$\varphi_{ce} = \frac{n\pi \cos \phi [\sin \bar{\alpha} + \sin \bar{\beta}]}{2 \tan \phi \cos \bar{\alpha}}, \quad (7.19)$$

where $s = d \cos^2 \phi$ as been invoked. Clearly, the center-edge interference phase is $\varphi_{ce} = 0$ for $\bar{\beta} = -\bar{\alpha}$ diffraction for all n . As before, the relative intensity for order n is the interference function modulated by the blaze function at each $\bar{\beta}$,

$$I(n, \bar{\beta}) = I_i(n) \cdot I_b(n, \bar{\beta}) = \frac{\sin^2 \left(\frac{n\pi \cos \phi [\sin \bar{\alpha} + \sin \bar{\beta}]}{2 \tan \phi \cos \bar{\alpha}} \right)}{\left(\frac{n\pi \cos \phi [\sin \bar{\alpha} + \sin \bar{\beta}]}{2 \tan \phi \cos \bar{\alpha}} \right)^2} \quad (7.20)$$

where

$$\lambda(n, \bar{\beta}) = \frac{d}{n} (\sin \bar{\alpha} + \sin \bar{\beta}), \quad (7.21)$$

is the wavelength at each $\bar{\beta}$ at order n .

Equations 7.20 and 7.21 provide the basic relationships for spectrograph design. A central choice of the design is, of course, the spectral dispersion (resolving power), which increases with increasing n/d . As such, the choice of n and d are critical. In the most general terms, spectrographs either work with lower dispersion in low orders, or in higher dispersions in higher orders. We discuss two example designs below.

7.1.2 Low Order Spectrographs

Low order gratings are generally blazed at $15^\circ \leq \phi \leq 20^\circ$ with $300 \leq 1/d \leq 1200$ facets mm^{-1} for orders $1 \leq n \leq 3$. It is desirable to have $\bar{\alpha} \sim \phi$. The blaze functions (Eq. 7.20) and solutions to the grating equation (Eq. 7.21) for a spectrograph with $\phi = 18^\circ$, $1/d = 600$ facets mm^{-1} , and $\bar{\alpha} = 22^\circ$ are illustrated in Fig. 7.6 for orders $n = 1, 2$, and 3 .

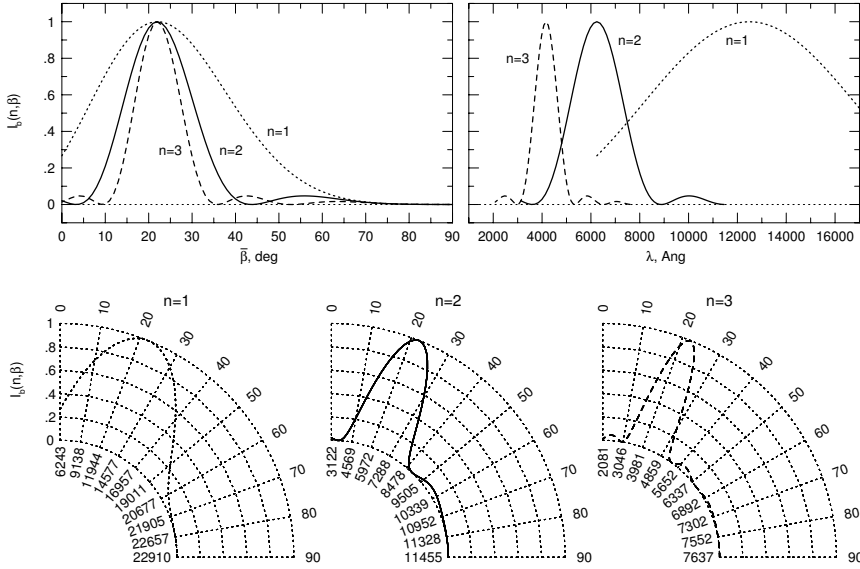


Figure 7.6: Solutions to Eqs. 7.20 and 7.21 for a spectrograph with at $\phi = 18^\circ$, $1/d = 600$ facets mm^{-1} , and $\bar{\alpha} = 22^\circ$, for orders $n = 1, 2$, and 3 . — (upper left) The dependence of the blaze functions on the diffraction angle, $\bar{\beta}$. — (upper right) The blaze functions with wavelength, λ . — (lower) The blaze functions shown in polar coordinate representation, which provides the spatial relationship between λ , $I_b(n, \bar{\beta})$, and $\bar{\beta}$.

As can be seen in the upper left panel of Fig. 7.6, the blaze functions peak at $\bar{\beta} = -\bar{\alpha} = 22^\circ$ for all n . Note that the angular width of the blaze function scale as $1/n^2$. Only the range $0^\circ \leq \bar{\beta} \leq 90^\circ$ is presented. In the upper right panel of Fig. 7.6, the wavelengths of the blaze peaks scale as $1/n$.

This example spectrograph is configured for an optical wavelength range of 4000–8500 Å in order $n = 2$ for a camera centered at $\bar{\beta} = 22^\circ$ that subtends roughly 20° ($10^\circ \leq \bar{\beta} \leq 30^\circ$). Although many of these wavelengths appear in multiple orders, examination of the lower panels of Fig. 7.6 reveals that they are diffracted toward different $\bar{\beta}$ for each n , which mitigates

confusion. Consider the $n = 2$ blaze center, $\lambda \simeq 6500 \text{ \AA}$ at $\bar{\beta} \simeq 22^\circ$. This wavelength is diffracted toward $\bar{\beta} \simeq 5^\circ$ for $n = 1$ and toward $\bar{\beta} = 55^\circ$ for $n = 3$. Both these diffraction angles reside well beyond the angular placement of the camera for $n = 2$.

Potential confusion can occur for $\lambda \leq 4860 \text{ \AA}$ from $n = 3$ spatially overlapping with $\lambda \geq 4860 \text{ \AA}$ from $n = 2$. In this case, a “high-pass” blocking filter that transmits $\lambda \geq 4860 \text{ \AA}$ would eliminate the confusion. As such, this example spectrograph design is not optimal for blue wavelengths.

7.1.3 Echelle Spectrographs

Echelle gratings can have a large range of ϕ , $\bar{\alpha}$, and d . However, some useful applications fall in the range of gratings blazed at $50^\circ \leq \phi \leq 70^\circ$ with $60 \leq 1/d \leq 80 \text{ facets mm}^{-1}$ for orders $20 \leq n \leq 100$. As with lower dispersion spectrographs, it is desirable to have the incident angle $\bar{\alpha} \sim \phi$. The blaze functions (Eq. 7.20) and solutions to the grating equation (Eq. 7.21) for an echelle spectrograph with $\phi = 52^\circ$, $1/d = 70 \text{ facets mm}^{-1}$, and $\bar{\alpha} = 70^\circ$ are illustrated in Fig. 7.6 for orders $n = 32$ –70.

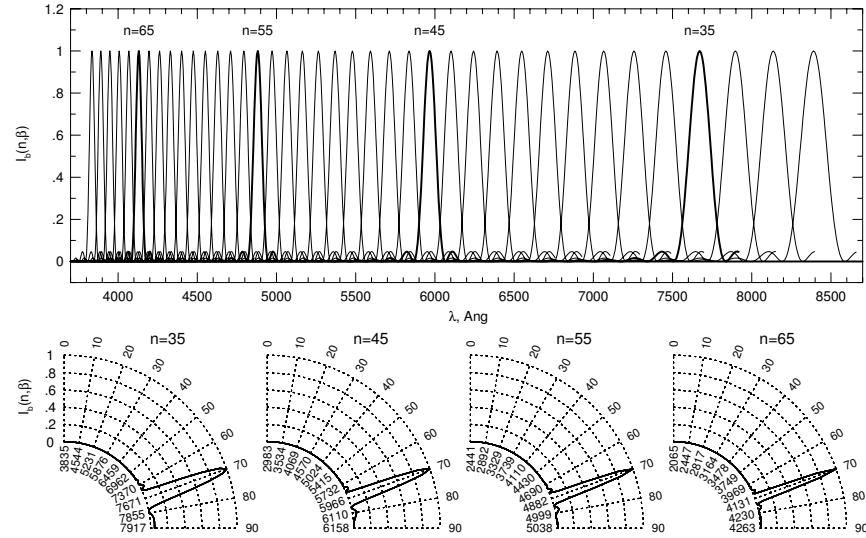


Figure 7.7: Solutions to Eqs. 7.20 and 7.21 for an echelle spectrograph with at $\phi = 52^\circ$, $1/d = 80 \text{ facets mm}^{-1}$, and $\bar{\alpha} = 70^\circ$, for orders $n = 32$ –70. — (upper) The blaze functions with wavelength, λ . — (lower) The blaze functions shown in polar coordinate representation (for $n = 35, 45, 55$, and 65), which provide the angular relationship between λ , $I_b(n, \bar{\beta})$, and $\bar{\beta}$.

In the upper panel of Fig. 7.7, the blaze functions are shown as a function of wavelength. Orders 35, 45, 55, and 65 are labeled. In the lower panels of Fig. 7.7, the angular relationships for these four orders are illustrated. As with the low resolution design presented above, the widths of the blaze function become narrower as $1/n^2$. However, what is most striking is that each blaze function covers a narrow range of wavelengths (high dispersion) and is spatially aligned at $\bar{\beta} = -\bar{\alpha} = 70^\circ$. For a camera and detector that are sensitive to the full optical and near-infrared range (4000–9000 Å), there will be significant confusion due to the spatial overlap of the wavelengths present in each order. For example, all wavelengths at the blaze peaks shown in the upper panel of Fig. 7.7 will overlap at $\bar{\beta} = 70^\circ$.

To spatially separate the echelle orders, a second grating, called a cross disperser, is placed in the light path following the echelle grating. The cross disperser operates at low order, usually $m_x = 1$, and thus has grating parameters that are similar to the low order spectrograph example in § 7.1.2. The cross disperser is configured at a right angle to echelle grating. Note that, if the cross disperser is a flat grating, the diverging light beam from the echelle grating must be recollimated, which can be accomplished with a refracting lens (though it is possible to use a concave grating for the cross disperser) to ensure an effective constant incident angle, α_x .

Consider a cross disperser grating with facet separations d_x blazed at ϕ_x operating in order m_x and oriented so that the post-echelle light is incident at angle α_x . The cross disperser will refract each wavelength into the direction β_x . Following the above convention, let $\bar{\alpha}_x = \alpha_x - \phi_x$ and $\bar{\beta}_x = \beta_x - \phi_x$ be the incident and refraction angles with respect to the cross disperser facet normals. The cross disperser introduces a two dimensional mapping of wavelength in the $\bar{\beta}_x$ – $\bar{\beta}$ plane (using the convention that the echelle grating has no subscript).

The diffraction angle off the cross disperser is

$$\sin \bar{\beta}_x = \frac{m_x}{d_x} \lambda(n, \bar{\beta}) - \sin \bar{\alpha}_x, \quad (7.22)$$

where $\lambda(n, \bar{\beta})$ is taken from Eq. 7.21 for the echelle grating. From Eq. 7.2, the mapping will have a tilt in the $\bar{\beta}_x$ – $\bar{\beta}$ plane given by

$$\tan \Psi(\bar{\beta}_x, \bar{\beta}) = \frac{d\bar{\beta}_x/d\lambda}{d\bar{\beta}/d\lambda} = \frac{m_x}{d_x} \frac{d}{n} \frac{\cos \bar{\beta}}{\cos \bar{\beta}_x}. \quad (7.23)$$

The cross dispersion is relatively constant (though not strictly) for a given echelle order (small $\bar{\beta}_x$ range) while the echelle dispersion is varying; as such the angle $\Psi(\bar{\beta}_x, \bar{\beta})$ will vary and the orders will have a slight curvature

in the $\bar{\beta}_x$ - $\bar{\beta}$ plane. At the blaze peaks, the order separation will be

$$\sin \bar{\beta}_x = 2 \frac{m_x}{m} \frac{d}{d_x} \sin \bar{\alpha} - \sin \bar{\alpha}_x, \quad (7.24)$$

which was obtained by substituting $\bar{\beta} = -\bar{\alpha}$ into Eq. 7.21.

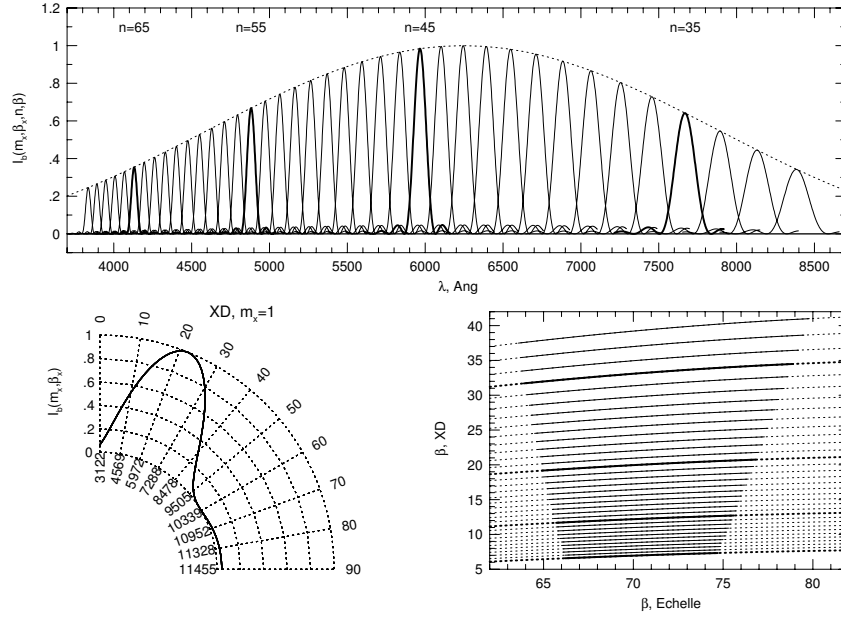


Figure 7.8: Solutions to Eqs. 7.20, 7.21, and 7.22 for the echelle grating illustrated in Fig. 7.7 after being cross dispersed in order $m_x = 1$ with a grating blazed at $\phi = 14^\circ$, $1/d = 1200$ facets mm^{-1} , and $\bar{\alpha} = 22^\circ$. — (upper) The dependence of the echelle blaze functions on wavelength, λ . The dotted curve is the cross disperser blaze function. — (lower left) The cross disperser blaze function shown in polar coordinate representation, which provide the angular relationship between λ , $I_b(m_x, \bar{\beta}_x)$, and $\bar{\beta}_x$. — (lower right) The mapping of the echelle orders, n , in the $\bar{\beta}_x$ - $\bar{\beta}$ plane. Wavelength increases from the lower left to the upper right; orders $n = 35$ with $\lambda_b = 7671$ Å, $n = 45$ with $\lambda_b = 5966$ Å, $n = 55$ with $\lambda_b = 4882$ Å, and $n = 65$ with $\lambda_b = 4131$ Å are presented as thick curves. The solid curves provide the free spectral range of each order.

The overall echelle blaze function is then the blaze function of the echelle grating modulated by the blaze function of the cross disperser,

$$I(m_x, \bar{\beta}_x, n, \bar{\beta}) = I(n, \bar{\beta}) \cdot I(m_x, \bar{\beta}_x) \quad (7.25)$$

where $I(n, \bar{\beta})$ and $I(m_x, \bar{\beta}_x)$ are the blaze functions for the echelle and cross disperser gratings obtained from Eq. 7.20.

The blaze functions (Eq. 7.20) and solutions to the grating equations (Eqs. 7.21 and 7.22) for a spectrograph with the above echelle grating parameters and a cross disperser with $\phi_x = 14^\circ$, $1/d_x = 1200 \text{ facets mm}^{-1}$, and $\bar{\alpha} = 22^\circ$ are illustrated in Fig. 7.8. The upper panel illustrates the modulation of the echelle blaze functions by the cross disperser blaze function (dotted curve). As in Fig. 7.7, orders $n = 35, 45, 55$, and 65 are shown as thick curves. The lower left panel illustrates the β_x dependence of the cross disperser blaze function and its wavelength range in polar coordinates.

The mapping of wavelength in the β_x - β plane is illustrated in the lower right panel of Fig. 7.8. The resulting mapping aligns the echelle orders in the β_x direction with the order dispersion mapped in the β direction. Longer wavelength orders are diffracted to larger β_x , so that wavelength increases from the lower left to the upper right in the β_x - β plane. Order $n = 35$, with blaze wavelength $\lambda_b = 7671 \text{ \AA}$ ($\beta = 70^\circ$) is centered at $\beta_x = 31^\circ$, where as order $n = 55$, with blaze wavelength $\lambda_b = 4882 \text{ \AA}$ is centered at $\beta_x = 12^\circ$. The free spectral range for each order is shown as the solid curves. Outside the free spectral range, a given wavelength is mapped in adjacent orders.

The main benefits of the echelle format is a large resolving power (high dispersion) with a large wavelength coverage while minimizing confusion; though it may be necessary to use a blocking filter for the shorter wavelengths due to second order dispersion from the cross disperser. If the orders are not well separated, a drawback of the echelle format is that background light from the sky may be difficult to sample. There can also be complications from scattered light from the many required optical elements.

7.1.4 Monochromatic Resolving Power

The monochromatic resolving power of a spectrograph depends upon the grating properties, and can be obtained from the grating equation (Eq. 7.1),

$$\varphi_{cc}(n) = \frac{n\lambda}{d} = \sin \alpha + \sin \beta, \quad (7.26)$$

where $\varphi_{cc}(n\pi)$ is defined as the center-to-center phase difference from reflection off of adjacent facets for integer multiples of π . As we showed in § 7.1.1.5, from the intensity function (Eq. 7.12) illustrated in Fig. 7.4, the width of the interference maxima is given by

$$\Delta\varphi_{cc}(n) = \frac{\lambda}{L}, \quad (7.27)$$

which also follows from the standard theorem of Fourier transforms that data sampled with a window Δ have frequency widths of $1/\Delta$; in this

case the length of the grating, L , (this is the same principle by which the diffraction limited resolving power of a telescope is λ/D , where D is the telescope diameter). Differencing the grating equation yields

$$\Delta\varphi_{cc}(n) = \frac{n}{d}\Delta\lambda. \quad (7.28)$$

Equating Eqs. 7.27 and 7.28 gives

$$\Delta\lambda = \frac{\lambda}{n} \frac{d}{L}. \quad (7.29)$$

The definition of the grating monochromatic resolving power is

$$R = \frac{\lambda}{\Delta\lambda} = n \frac{L}{d}, \quad (7.30)$$

which is a constant with wavelength for a given spectral order, and grating configuration, depending only upon the ratio of the facet length to the grating length (equals the number of facets, N_f).

In practice, the resolution of a spectrograph is lower than the monochromatic resolution of the grating. The spectral resolution is dominated by the spectral purity, which is a measure of the width of a monochromatic image of the slit.

7.1.5 Spectral Purity

Consider a monochromatic light source with an image that fills the slit as seen from the collimator. Light from one edge of the slit strikes the collimator, and therefore the grating, with a slightly different incident angle, α , than light from the other edge of the slit. If the slit width is w , then the angular size at the collimator, and therefore the range of incident angles on the grating is

$$d\alpha = \frac{w}{f_{coll}}. \quad (7.31)$$

The spectral purity is the spatial broadening of the monochromatic image of the slit at the detector (camera focal plane). That is, it is the linear dispersion in wavelength at the detector for a chromatic wavefront due to the small range of reflection angles off the grating. The range of reflection angles, $d\beta$, off the grating are due to the range of incident angles, $d\alpha$, due to the finite slit width, w . The relationship between $d\alpha$ and $d\beta$ follows from the grating equation, Eq. 7.1,

$$\frac{n}{d}d\lambda = \cos\alpha d\alpha + \cos\beta d\beta, \quad (7.32)$$

which, for a monochromatic source, i.e., $d\lambda = 0$, gives

$$d\beta = -\frac{\cos \alpha}{\cos \beta} d\alpha. \quad (7.33)$$

In physical coordinates, x , the size of the image of the slit at the detector focal plane is given by the relation

$$dx = f_{cam} d\beta, \quad (7.34)$$

which gives the width of the image of the slit, w' ,

$$w' = f_{cam} d\beta = -f_{cam} \frac{\cos \alpha}{\cos \beta} d\alpha = -w \frac{f_{cam}}{f_{coll}} \frac{\cos \alpha}{\cos \beta}, \quad (7.35)$$

where Eqs. 7.33 and 7.31 have been substituted for $d\beta$ and $d\alpha$, respectively. The ratio w'/w is the magnification in the dispersion direction; as mentioned above, the ratio f_{cam}/f_{coll} is the magnification in the spatial direction. Note that the image is inverted.

The conversion of the physical coordinates, x , of the slit image on the focal plane (detector) into dispersion coordinates, λ , is given by

$$\Delta\lambda = w' \frac{d\lambda}{dx} = w' \frac{d\lambda}{d\beta} \frac{d\beta}{dx} = \frac{w'}{f_{cam}} \frac{d\lambda}{d\beta}, \quad (7.36)$$

where Eq. 7.34 has been substituted for $d\beta/dx$. From Eq. 7.32, we have the angular dispersion

$$\frac{d\lambda}{d\beta} = \frac{d}{n} \cos \beta, \quad (7.37)$$

which, after substitution into Eq. 7.36, and substituting Eq. 7.35 for w' , gives the spectral purity

$$\Delta\lambda = -\frac{w}{f_{coll}} \frac{d}{n} \cos \alpha. \quad (7.38)$$

Smaller $\Delta\lambda$ is desired, but there are practical trade offs. It is clear that one would like to work with α approaching $\pi/2$ at high orders. These two consideration requires a larger facet angle, ϕ . Also, smaller facet spacings, d , are desirable. A narrower slit width decreases $\Delta\lambda$, but the trade off is that if the width is narrower than the atmospheric seeing (assuming a point source), there is light loss at the slit. A long collimator focal length is often a viable solution, but this will require a long light path and a large collimator and grating size.

The actual limiting resolution of the spectrograph is then obtained from the ratio of the grating equation (Eq. 7.1) to the spectral purity (Eq. 7.38), giving the general expression,

$$R = \frac{\lambda}{\Delta\lambda} = \frac{f_{coll}}{w} \frac{n^2}{d^2} \left(\frac{\sin \alpha + \sin \beta}{\cos \alpha} \right). \quad (7.39)$$

Note that the resolution is maximized for a narrow slit and a long collimator focal length. It is important, however, to consider the physical pixel size on the detector. It is a poor design to under sample or oversample $\Delta\lambda$. The former yields a loss of information, and the latter must be paid for by longer observations. We touch on these issues below.

7.1.6 Instrumental Spread Function

As discussed in §§ 7.1.4 and 7.1.5, the amount of dispersion of the light is characterized by the resolution

$$R = \frac{\lambda}{\Delta\lambda}, \quad (7.40)$$

where $\Delta\lambda$ is the spectral purity given by Eq. 7.38. The spectral purity describes the “blurring” of monochromatic beams on the detector. In practice, the *distribution* of this blurring can be a complex function, called the instrumental spread function (ISF). The quantity $\Delta\lambda$ quantifies the full-width half-max (FWHM), of the ISF. For a well-behaved spectrograph, the ISF can be approximated as a normalized, symmetric Gaussian function,

$$\Phi(\lambda' - \lambda) = \frac{1}{\sqrt{2\pi}\sigma} \exp \left[-\frac{(\lambda' - \lambda)^2}{2\sigma^2} \right], \quad (7.41)$$

where $\sigma = \Delta\lambda/2.35$, and where $\Delta\lambda$ is the FWHM of a monochromatic light beam. The interpretation of Eq. 7.41 is that counts of monochromatic light at wavelength λ will include counts from monochromatic light at wavelength λ' in proportion to $\Phi(\lambda' - \lambda)$.

The term $\Delta\lambda$ is often called the *resolution element*. Very narrow features, such as narrow absorption lines, will have the shape of $\Phi(\lambda' - \lambda)$. That is, they will have $\text{FWHM} = \Delta\lambda$. Such features are called *unresolved lines*. Note that the FWHM of an unresolved line is dependent upon the observed wavelength in the spectrum. The *observed* widths of unresolved lines get broader in direct proportion to wavelength, i.e., $\Delta\lambda \propto \lambda$.

Typically, the ISF is determined by Gaussian fitting sky lines at various intervals in wavelength across the spectral format. However, the sky is an extended source, not a point source like the quasar. In some cases,

the location of the source on the slit can modify the shape of the ISF, including asymmetries in the shape that can change with wavelength. For example, not placing the slit at the parallactic angle (perpendicular to the horizon) can result in seeing disks at different wavelengths to have slightly shifted spatial locations across the slit. This will result in the blue wing of the ISF to be truncated at shorter wavelengths and the red wing to be truncated at longer wavelength, while the profile is symmetric at intermediate wavelengths. In these cases, fitting the sky lines will provide an ISF profile that is not applicable to the data.

7.1.7 ISF Convolution

Consider a wavelength range comprising an absorption line with a profile shape given by

$$I_{\lambda} = I_{\lambda}^o \exp[-N\alpha(\lambda)] = I_{\lambda}^o \exp(-\tau_{\lambda}) \quad (7.42)$$

where N is the column density of atoms, $\alpha(\lambda)$ is the absorption coefficient per atom, given by Eq. 5.17, and τ_{λ} is the line absorption optical depth, defined as in Eq. 5.3.

The incoming beam intensity is modified by a convolution of the instrumental spread function (ISF) with the absorption profile. In the region of a spectral line, the intrinsic line shape will be modified following

$$\hat{I}_{\lambda} = \Phi(\lambda' - \lambda) \otimes I_{\lambda}^o \exp(-\tau_{\lambda}), \quad (7.43)$$

where \hat{I}_{λ} is the observed counts prior to pixelization (see § 7.1.8). Often the ISF is approximated as a Gaussian function, though some instruments have ISF profiles that significantly depart from this shape. An explicit writing of Eq. 7.43 is

$$\hat{I}_{\lambda} = \int_{-\infty}^{\infty} \Phi(\lambda' - \lambda) I_{\lambda'}^o \exp(-\tau_{\lambda'}) d\lambda', \quad (7.44)$$

which must be evaluated at each λ to obtain the observed line shape.

In Fig. 7.9, an narrow pair of absorption lines observed at $\lambda = 2800 \text{ \AA}$ (left panel) is convolved with Gaussian representations of the ISF for five typical spectral resolutions, $R = 1000, 5000, 10,000, 20,000$, and $50,000$ (center panels). The FWHM is $\Delta\lambda = \lambda/R$. The observed profiles are presented in the right hand panels for each resolution. All panels are given in relative wavelength units from λ . Note that the $R = 1000$ panels cover a broader relative wavelength scale. Vertical dot-dot lines provide a guide for the eye to the location of the wavelength extent of the intrinsic profile. In this example, the intrinsic line widths are very narrow, $b = 5 \text{ km s}^{-1}$,

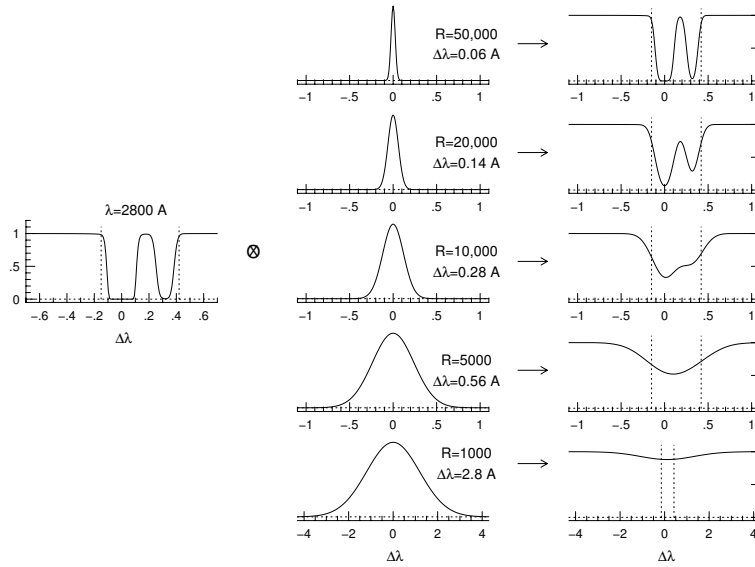


Figure 7.9: — Examples of ISF convolution with five commonly used spectroscopic resolutions, $R = 1000, 5000, 10,000, 20,000$, and $50,000$, with resolution increasing from the lower to the upper panels. The intrinsic profile entering the spectrograph is plotted to the left in relative wavelength units, centered at 2800 \AA . The Gaussian ISF profiles are plotted in the center panels. The $\Delta\lambda$ (FWHM) is labeled for each. Note the different scales for relative wavelength for presentation purposes. The observed profiles for each resolution are plotted in the right hand panels with the same relative wavelength scales. Vertical lines at $\Delta\lambda = -0.15$ and 0.42 provide the lower and upper wavelength range of the intrinsic profile for this example. A Mg II $\lambda 2796$ transition was assumed with two components. The components have column densities $\log N(\text{Mg II}) = 14.5$ and 13.0 cm^{-2} and both have $b = 5 \text{ km s}^{-1}$.

and this results in an almost complete “washing out” of the absorption line in the $R = 1000$ case. As resolution increases, the shape of the observed profile approaches the shape of the intrinsic profile.

From this example, it becomes quite clear how important the choice of spectral resolution is for the science objectives. Low resolution can result in non-detections (once noise and pixelization sampling are accounted for). Note the slight offset of the profile center in the $R = 5000$ case. Though the double nature of the line profile begins to appear at $R = 10,000$, it is not until $R = 20,000$ that the observed profile takes on a shape approaching the intrinsic profile. It is also important to realize that even for a saturated profile, where the counts are zero in the intrinsic line core, that the counts in the observed profile are not zero. Not until $R = 50,000$ is there any real

hope of constraining the intrinsic line widths.

7.1.8 Pixelization

Due to the nature of CCD detectors, the intensity profile (following convolution with the ISF), is sampled in discrete pixels. The process of pixelization is mathematically equivalent to multiplying the convolved profile with an infinite series of delta functions

$$III(x) = \sum_{k=-\infty}^{\infty} \delta(x - k\Delta x), \quad k = \text{integer}, \quad (7.45)$$

where Δx is the spacing between pixels. This function is the well-known Shah function. Each of these pixels has a width, ranging from $-\Delta x/2$ to $\Delta x/2$, which are known as the data windows. These data windows are a series of box functions, $B(x)$, centered on each of the δ functions appearing in the Shaw function.

Thus, the sampled observed data are given by

$$I_\lambda = B(\lambda)III(\lambda)\hat{I}_\lambda, \quad (7.46)$$

where \hat{I}_λ is given by Eq. 7.43. Note that the Shah function in x coordinates and the box widths, Δx , are fixed by the physical pixel sizes. How they translate to wavelength and wavelength widths depends upon the spectrograph design, according to Eqs. 7.34 and 7.37, giving

$$\frac{d\lambda}{dx} = \frac{d \cos \beta}{n f_{cam}}. \quad (7.47)$$

The λ coordinate will not be at equal x intervals nor have equal wavelength widths due to the dispersive nature of spectra. Recall that, at any wavelength location in the spectrum, a $\Delta\lambda$ interval is proportional to λ/R .

The sampling rate is described by the number of pixels per resolution element, $\Delta\lambda = \lambda/R$, defined as

$$p = \frac{\Delta\lambda}{\Delta\lambda(x)} = \frac{\lambda/R}{\Delta\lambda(x)}, \quad (7.48)$$

where $\Delta\lambda(x)$ is the wavelength extent of a single pixel at x . In Fig. 7.10, the pixelization of an unresolved absorption line with $R = 8000$ at $\lambda = 2796.352$ (left panel) is illustrated for four integer values of p . The center panels illustrate the Shah function, $III(\lambda)$, for $p = 1, 2, 3$, and 4 (lower to upper). The right panels show the resulting sampled profile for each p . The Shah function has been centered on the absorption line; for $p \leq 2$, the sampled

absorption line shape is sensitive to where the line centroid falls with respect to the center of $B(\lambda)$.

Technically, an absorption intrinsic profile cannot be reconstructed by deconvolution of the ISF from the pixelized data when $p \leq 2$. This follows from the Nyquist frequency, below which aliasing of the original input signal occurs. In practice, deconvolution of the data is rarely attempted, mainly because there are more robust and competitive methods for extracting the intrinsic profile shape of noisy data. We discuss the an approach to quantifying the noise in the data in § 7.2.3.1.

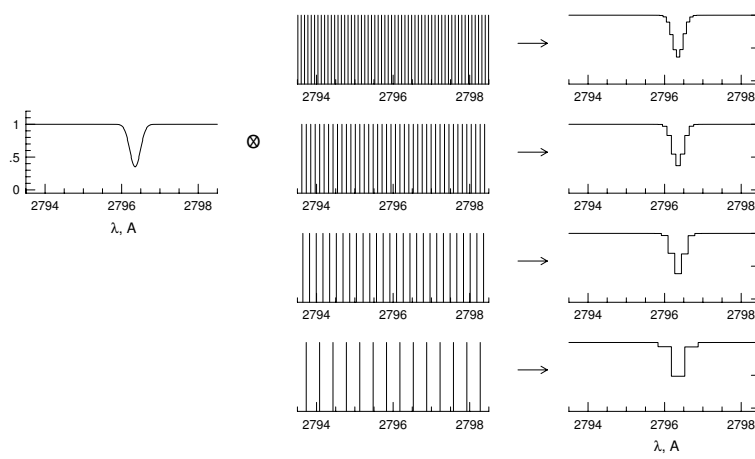


Figure 7.10: — Examples of pixelization for an $R = 8000$ unresolved absorption line at $\lambda = 2796.352$ (left panel) for four different sampling rates. — (center) The Shah function, Eq. 7.45, for sampling rates corresponding to $p = 1, 2, 3$, and 4 . $\Delta\lambda(x) = p\Delta\lambda$, where $\Delta\lambda = \lambda/R$ is the resolution element. — (right) The sampled spectra for each p .

7.2 Extracting the Data

7.2.1 Charged Couple Devices

The CCD counts photons by collecting electrons in each CCD pixel, which is a potential well where the electrons are stored. CCDs are well suited for counting incoming photons because they have high quantum efficiency and a linear response; the number of electrons stored in each potential well is directly proportional to the number of photons striking the pixel. Following the collection of electrons in the potential wells, the camera shutter is closed and the CCD is read out column by column. Each column is “moved” to

a register, which is then read out in row order. The resulting data are stored digitally in a two-dimensional array that provides the “image” of the spectrum. Each stored image is called a “frame”.

The read out amplified converts the number of electrons, which are measured as an analog current, into a digital number. The conversion between the digital number, DN, and the number of electrons, N_e , registered in each pixel is called the gain, expressed

$$g = \frac{N_e}{\text{DN}}. \quad (7.49)$$

A typical value for the gain ranges from $\simeq 2$ –5, depending upon the electronic controller settings. Associated with each pixel is an uncertainty due to the measuring of the current, which is called the read noise, RN. Typical values of RN range from a few to several electrons. There is also a small discretization uncertainty on the order of one electron that is usually insignificant.

The nature of the read out process is that it requires current to measure current. Thus, the resulting digital number provided by the system is the sum of the electrons detected and the electrons used to count them; the data are raised on a “pedestal”. The magnitude of this pedestal is determined by reading blank registers before the CCD read out is started and/or after the CCD read out is completed. These blank registers are also stored in the two-dimensional “image” and are called the prescan and overscan regions, respectively. Sometimes, there is the option to bin the CCD during the read out process. If this is done, it is important to recognize that the gain and read noise will be different than if there is no binning.

There are additional noise sources, both additive and multiplicative. If the electronics are not stable, have fixed pattern noise, or exhibit hysteresis, then this additive noise source must be removed by subtracting out the noise pattern. Usually, this is accomplished by acquiring a series of “zero” frames. With the camera shutter closed, the CCD is fully read out. To reduce the pixel to pixel noise, several to ten zero frames are acquired and then averaged. A multiplicative noise source arises due to the pixel to pixel quantum efficiency variations, or fixed illumination patterns due to dust, etc., on the CCD. These variations are usually corrected by obtaining “flat field” frames. Flat fields are normally obtained by taking spectra of smooth continuous light sources, such as quartz lamps. As with the zero frames, usually several to ten flat frames are acquired and then averaged to beat down the pixel to pixel noise.

The wavelength dispersion solution (i.e., pixel versus wavelength) is obtained by taking a spectrum of an emission line source, usually an excited HeNe or a ThAr lamp.

7.2.2 Reducing the Data Suite

For the following discussion, it is assumed that a data suite consisting of data, comparison lamps, zero, and flat field frames has been obtained for the spectroscopic observations. Dark current will be ignored, but note that it can be treated in a manner similar to the zero frame, since it is an additive contribution to the data.

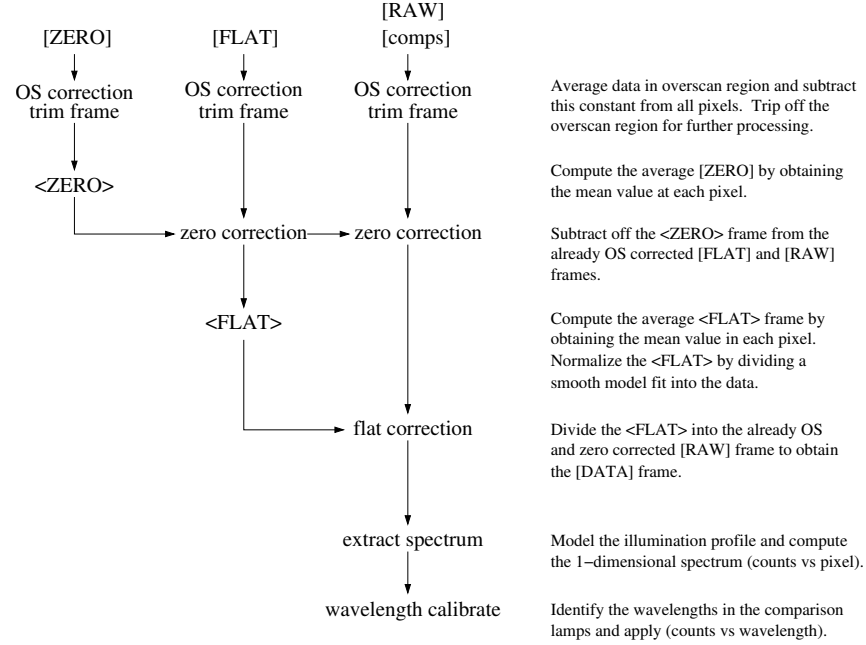


Figure 7.11: — A schematic flow chart showing the steps outline for the reduction of the data suite. For simplicity of illustration, the scattered light subtraction is omitted and the comparison lamps are treated as [RAW] frames.

Each observed [RAW] data frame must be overscan subtracted, zero frame corrected, scattered light corrected and flat field corrected in a series of additive and multiplicative calibration steps. The desired data frame, [DATA], is convolved with instrumental “information” according to

$$[\text{RAW}] = \left\{ [\text{DATA}] + [\text{SCATTER}] \right\} \langle \text{FLAT} \rangle + \langle \text{ZERO} \rangle + \text{OS}, \quad (7.50)$$

where OS is the overscan electronic pedestal of the [RAW] frame, the FLAT term is the pixel to pixel variations due to non-uniform detector quantum

efficiency, the ZERO accounts for two-dimensional fixed pattern due to the detector read out process, and the [SCATTER] frame is the scattered light within the spectrograph. The OS and ZERO corrections are applied to each individual frame, where the former are often a constant or a smooth function. Uncertainty in the OS level results only in a zero point offset for each frame. If there is an offset, it is usually corrected to first order by the ZERO correction. When the electronics are stable, the noise in the individual [ZERO] and [FLAT] frames can be reduced by averaging them,

$$\langle \text{ZERO} \rangle = \frac{1}{N_z} \sum_{i=1}^{N_z} ([\text{ZERO}]_i - \text{OS}_i), \quad (7.51)$$

$$\langle \text{FLAT} \rangle = \frac{1}{N_F} \sum_{i=1}^{N_F} \{([\text{FLAT}]_i - \text{OS}_i) - \langle \text{ZERO} \rangle\}, \quad (7.52)$$

where N_z and N_F are the number of zero and flat field frames obtained in the calibration suite. The mean $\langle \text{FLAT} \rangle$ frame can then be normalized to unity, but this is not necessary, depending upon individual approaches to data calibration. Scattered light can often be negligible, but when it is not, a smooth scattered light model can be obtained and recorded as a scattered light frame, [SCATTER]. Each calibrated data frame [DATA] is then obtained by

$$[\text{DATA}] = \frac{([\text{RAW}] - \text{OS}) - \langle \text{ZERO} \rangle}{\langle \text{FLAT} \rangle} - [\text{SCATTER}]. \quad (7.53)$$

It is this frame from which the spectrum is extracted.

7.2.3 Extracting the Spectrum

The extraction of the spectra can be optimized using the algorithms of Horne (1986) and Marsh (1989). Their algorithms are designed to best determine the fraction of flux that falls into each *dispersion* pixel (at every wavelength) of the spectrum. This is achieved by optimally weighting the flux values in each *cross dispersion* pixel used in the extraction sum. This minimizes statistical noise and maximizes photometric accuracy.

Optimal extraction can be illustrated as follows. Consider an image of a an illumination profile with cross dispersion direction pixels i (also called the spatial direction) and dispersion direction pixels j . Given the following definitions: I_j = the extracted counts in pixel j (before wavelength calibration), I_{ij} = the signal counts, B_{ij} = the background counts (i.e. the sky, scattered light, etc.), and P_{ij} = the spatial probability profile. where the B_{ij} are selected in regions where $P_{ij} = 0$. For proper statistical treatment, all defined values must be in units of electrons (this means that the

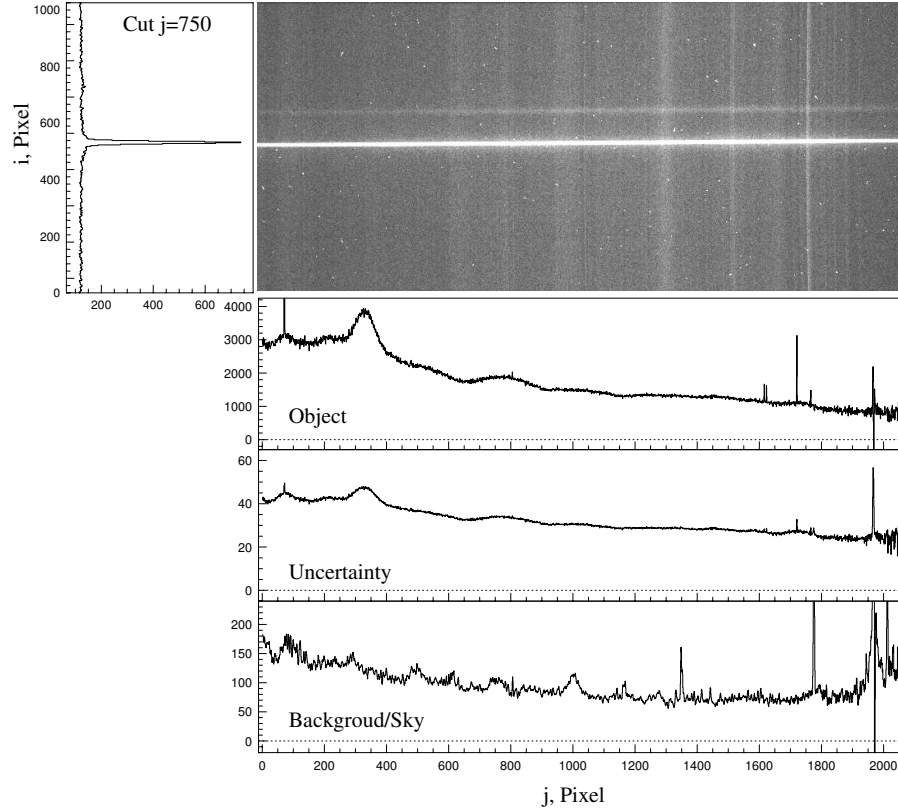


Figure 7.12: — A longslit spectrum showing a cross-cut at along the spatial direction, i , and the extracted spectrum (Eq. 7.59), the uncertainty spectrum (Eq. 7.61), and the background/sky spectrum (straight sum) along the dispersion direction, j .

image should be multiplied by the detector gain prior to extraction). The probability profile is normalized to unity,

$$P_j = \sum_{i=1}^{N_i} P_{ij} = 1, \quad (7.54)$$

where N_i is the number of pixels used to characterize the illumination profile in the spatial direction. The P_{ij} give the probability that a photon with dispersion pixel j is registered in the spatial i . It is possible to obtain the P_{ij} by fitting Gaussian or generalized functions to the illumination profile in the spatial direction. The shape and width will depend upon how well the image of the quasar was centered on the slit and the atmospheric seeing.

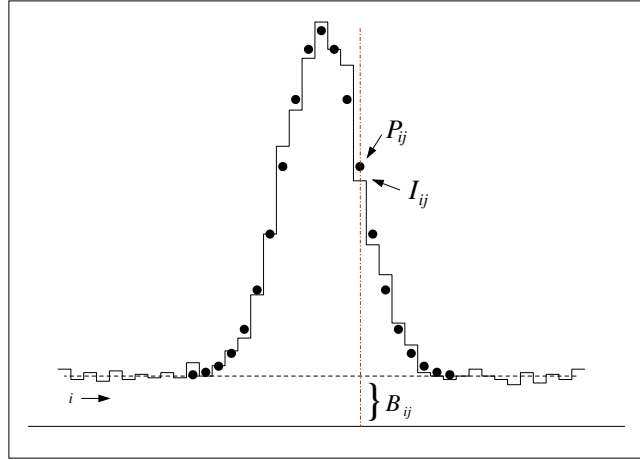


Figure 7.13: — A schematic of a spatial cross cut of the illumination profile at a fixed wavelength location (fixed j). The data, I_{ij} , are the thin line, including noise and background counts. The background is modeled with a smooth curve fit through regions beyond the illumination profile. The values of the fitted probability profile are the solid dots.

For any given pixel i at each j , the value of I_j is the scaled value

$$I_j = \frac{I_{ij} - B_{ij}}{P_{ij}} \equiv D_{ij} \quad (7.55)$$

if no noise is present. When noise is present, the D_{ij} provide independent estimates of the I_j for every pixel with $P_{ij} > 0$. As such, the extracted counts can be expressed as the linear combination of the D_{ij} in the spatial direction:

$$I_j = \frac{\sum_{i=1}^{N_i} w_{ij} D_{ij}}{\sum_{i=1}^{N_i} w_{ij}}, \quad (7.56)$$

where w_{ij} is the weighting factor. In Figure 7.13, a schematic of the cross dispersion profile is shown at a fixed j . The solid dots provide the estimated illumination profile shape, the P_{ij} . In practice, the background is estimated by a smooth functional fit in the spatial direction at each j (horizontal dashed line) to regions outside the illumination profile. The smooth

background, B_{ij} , is subtracted off the I_{ij} and this quantity is divided by P_{ij} in order to obtain an independent estimate of the total counts at the illumination profile peak.

From basic error analysis theory, this is achieved when the w_{ij} are chosen to be $1/\sigma_{D_{ij}}^2$, where

$$\sigma_{D_{ij}}^2 = \frac{V_{ij}}{P_{ij}^2}, \quad (7.57)$$

where V_{ij} is the variance due to Poisson statistics in D_{ij} . We will discuss the variance model in more detail in § 7.2.3.1. The weights are then,

$$w_{ij} = \frac{P_{ij}^2}{V_{ij}}, \quad (7.58)$$

and the optimal value of I_j is then given by

$$I_j = \frac{\sum_{i=1}^{N_i} \frac{P_{ij}}{V_{ij}} (I_{ij} - B_{ij})}{\sum_{i=1}^{N_i} \frac{P_{ij}^2}{V_{ij}}}, \quad (7.59)$$

with

$$V_j = \sigma_{I_j}^2 = \left(\sum_{i=1}^{N_i} \frac{P_{ij}^2}{V_{ij}} \right)^{-1}. \quad (7.60)$$

Often, the variance, V_{ij} , used in the above treatment is taken to be Poisson fluctuations, i.e. \sqrt{N} , model plus read noise, expressed as

$$V_{ij} = I_{ij} + B_{ij} + \text{RN}^2, \quad (7.61)$$

where RN is the read noise. However, this simplistic treatment commonly results in a variance spectrum, V_j , that is an underestimate of the distribution of noise in the extracted counts, I_j . In fact, there are additional statistical noise sources due to the additive and multiplicative calibration steps involved in preparing the raw data for the extraction process. There can also be fix pattern noise sources, such as dark current. Careful accounting based upon the actual reduction procedure to obtain the V_{ij} would be ideal.

7.2.3.1 The Variance Spectrum

The importance of an accurate estimate of the variance, or uncertainty, in the measured counts in each pixel cannot be overstated. The statistical

significance of virtually every measurement is computed directly from the variance spectrum, V_j . Beyond the simple Poisson plus read noise model, additional statistical uncertainty in the extracted spectrum arises during the detector calibration steps.

The variance model should then include each of the calibration steps of the data suite reduction outline in § 7.2.2 and illustrated in Figure 7.11. Invoking the notation of the operations

$$[\text{DATA}] = \frac{([\text{RAW}] - \text{OS}) - \langle \text{ZERO} \rangle}{\langle \text{FLAT} \rangle} - [\text{SCATTER}], \quad (7.62)$$

a pixel with calibrated data value at pixel ij , where i is the spatial direction and j is the dispersion direction, is expressed

$$d_{ij} = \frac{r_{ij} - z_{ij}}{f_{ij}} - \bar{s}_{ij}, \quad (7.63)$$

where d_{ij} , r_{ij} , z_{ij} , f_{ij} are the calibrated data counts, the raw counts, the zero counts in the mean zero frame, and the flat field counts in the mean flat field frame in pixel ij , respectively, and where \bar{s}_{ij} is the smooth scattered light model value in pixel ij . The OS correction to each quantity is implied. Recall that for proper statistical accounting, all frames should be multiplied by the gain to convert all values into units of electrons counted.

The variance in pixel ij is then

$$V_{ij} = \frac{1}{f_{ij}^2} \left[\sigma_{r_{ij}}^2 + \sigma_{z_{ij}}^2 + \left(\frac{r_{ij} - z_{ij}}{f_{ij}} \right)^2 \sigma_{f_{ij}}^2 \right] \quad (7.64)$$

where

$$\begin{aligned} \sigma_{r_{ij}}^2 &= r_{ij} + \text{RN}^2 \\ \sigma_{z_{ij}}^2 &= \frac{1}{n} \sum (z_k - \langle z_{ij} \rangle)^2 \\ \sigma_{f_{ij}}^2 &= \frac{1}{n} \sum (f_k - 1)^2 + \sigma_{z_{ij}}^2 \end{aligned} \quad (7.65)$$

where the sums are taken over a well-chosen region of n pixels centered on ij , and where

$$\langle z_{ij} \rangle = \frac{1}{n} \sum z_k, \quad (7.66)$$

summed over the same region. Poisson fluctuations have been assumed for the variance in the raw counts.

The above treatment provides reasonable estimates for the uncertainties introduced during the calibration of the data by direct computation of the

scatter in adjacent and close proximity pixels in the raw, data, and flat field frames. It has been assumed that the mean flat field frame has been normalized, so that the mean f_k is unity. Note, however, that the individual f_{ij} appearing in Eq. 7.64 are not necessarily unity.

Eq. 7.64 should be substituted for V_{ij} into Eqs. 7.59 and 7.60 appearing in § 7.2. However, since the quantity being weighted in Eq. 7.59 is $I_{ij} - B_{ij}$, the substitution is

$$V_{ij} = V(I_{ij}) + V(B_{ij}), \quad (7.67)$$

where $V(I_{ij})$ and $V(B_{ij})$ are taken from Eq. 7.64. Note that the probability profile in Eqs. 7.59 and 7.60 weights the V_{ij} most heavily in the extremes of the spatial direction at pixel j . However, also note that the dominant term in V_{ij} is $\sigma_{r_{ij}}^2$, where the illumination profile peaks.

7.2.3.2 Fixed Pattern Noise

There are times when fixed pattern noise is present in the detector, rendering a Poisson model inaccurate in certain regions of the spectrum. For example, dark current can be troublesome in so-called “hot” pixels. In regions where it is difficult to compute an accurate variance model during the extraction process, the data can be used directly. From the standard maximum likelihood method (assuming the errors are normally distributed), the variance due to fixed-pattern noise, $\hat{\sigma}_{I_j}^2$, in the j th pixel can be estimated as

$$\hat{\sigma}_{I_j}^2 = \frac{1}{N_p} \sum_{i=j_1}^{j_2} (I_i - I_i^c)^2, \quad (7.68)$$

from the extracted spectrum, where $N_p + 1$ pixels are used in estimation, $j_1 = j - N_p/2$, and $j_2 = j + N_p/2$. The sum is centered on pixel i and obvious absorption or emission features are excluded. Note that this treatment provides the mean variance in I_i about the continuum fit in the nearby pixels of the spectrum. The results from Eq. 7.68 can be sensitive to the choice of N_p , and the level of this sensitivity should be examined.

This method can also be invoke in cases where a data suite is not available for proper statistical treatment of the variance.

7.2.4 Wavelength Zero-Point

It is convention in the field of quasar absorption lines to calibrate the wavelength scale to vacuum wavelengths and then to apply a heliocentric correction. The use of vacuum wavelengths ensures that there is not an unphysical “stretching” of the spectrum in proportion to wavelength. This would have

the undesirable effect of elevating absorber redshifts in proportion to observed wavelength. It would also induce velocity shifts between different transitions from the same absorbers, also in proportion to the observed wavelength. These two steps place the observed redshifts of absorption systems on a heliocentric velocity zero-point.

It is easiest to simply identify calibration lines in emission line lamps using vacuum wavelengths, which avoids applying a correction to the calibrated spectrum. Lists of vacuum wavelengths are normally generated from laboratory measurements of air wavelengths that are then converted to vacuum. If air wavelengths are utilized, then a conversion to vacuum can be made using the same standard formulae used to generate the vacuum wavelengths. The conversion to vacuum wavelengths, λ_{vac} is then

$$\lambda_{vac} = \frac{1}{n} \lambda_{air}, \quad (7.69)$$

where λ_{vac} and λ_{air} are both measured in angstroms. A commonly used expression for the index of refraction, n , is given by the Cauchy dispersion formula,

$$n = 1 + 10^{-7} \left[2726.43 + \frac{12.288}{10^{-8} \lambda_{air}^2} + \frac{0.3555}{10^{-16} \lambda_{air}^4} \right], \quad (7.70)$$

where λ_{air} is the air wavelength for an environment of 15° C at atmospheric pressure.

The heliocentric correction is quite easily made from the formula

$$\lambda_h = \left(1 + \frac{v_h}{c}\right) \lambda_{vac}, \quad (7.71)$$

where v_h is the heliocentric velocity of the telescope at the time the quasar spectrum is obtained. The computation of v_h is quite involved and beyond the scope of this discussion.

7.2.5 Flux Calibration

The observed counts at each wavelength of a quasar spectrum will not follow the spectral energy distribution (SED) of the quasar because the transmission of photons through the atmosphere, telescope, and spectrograph, and the quantum efficiency (sensitivity) of the CCD are wavelength dependent. Flux calibration is the step that converts the observed counts versus wavelength spectrum into a flux versus wavelength spectrum. It both recovers the SED of the quasar and converts the counts into flux units. If done properly, multiple observations of the same object should have identical SEDs with identical flux counts in each wavelength pixel.

The three main phenomena that modify the incoming SED are:

- Atmospheric Extinction: Extinction through the atmosphere, which is greater in the blue, reduces the counts in the blue relative to the red. The degree to which this occurs depends upon the pathlength of atmosphere at the time of observation. The pathlength through the atmosphere, $\sec Z$, is referred to as “airmass”, where Z is the angle to the object measured from the zenith at the time of observation.
- Telescope/Spectrograph Transmission: The telescope mirrors and the spectrograph optical elements do not reflect or transmit all wavelengths with equal efficiency. Often a telescope facility–instrument combination will be optimized for a limited region of the spectral coverage. This shape of this transmission function can be very complex for echelle spectrographs, peaking at the blaze wavelength of each spectral order.
- CCD Efficiency: CCDs often have a “sweet spot” in the wavelength range where the efficiency at which incident photons are converted into electrons is highest. This region is often in the range of 5000–8000 Å. Below 4000 Å and above 9000 Å, CCD efficiencies usually drop very rapidly.

The combined effect of atmospheric extinction, telescope–instrument transmission, and CCD efficiency is called the throughput. The throughput is calibrated out of the data (counts versus wavelength) by observing so-called “standard stars”. These stars have well measured SEDs for which the flux zero points have been determined at each wavelength. In principle, to flux calibrate one’s quasar spectra, standard stars are observed with conditions as similar as possible to those for which the quasars are observed. The standard star spectra are extracted following the same procedures as for the quasar spectra. Then the SED of the standard star, usually obtainable from a library of standard star SEDs, is divided into the standard star spectrum and heavily smoothed to obtain the throughput curve. This smooth throughput curve is then multiplied into the quasar spectra. Care must be taken that the observing conditions are considered to be “photometric”, where the atmospheric transparency is effectively 100% (i.e., no clouds).

Flux calibration of quasar spectra is not always necessary. If the science objectives are simply to measure the properties of absorption lines, then flux calibration is not required because absorption is quantified relative to the continuum; the flux calibration divides out. However, if properties of the quasar spectrum itself are part of the science goals, then flux calibration is necessary. For example, one may wish to measure the spectral index, broad–

band magnitude, or reddening of the quasar. Note that flux calibration does not correct for Galactic reddening.

Flux calibration with echelle spectra is more challenging than calibration of long slit spectra. This is because the blaze function of the echelle cross disperser peaks at the blaze wavelength of each order. Along the echelle format, there can be regions where there are gaps in the spectral coverage and in other locations the spectral coverage can overlap from adjacent orders. Since the blaze function (Eq. 7.10) differs for each order, it is common that the flux calibration will yield unmatched flux values in these regions of spectral overlap. Care must be taken.

7.2.6 Continuum Fitting

The continuum fit is critical. Virtually all measurements will depend upon the ratio I_λ/I_λ^c , where I_λ is the counts and I_λ^c is the continuum model at wavelength λ , respectively. The placement of the continuum model, usually a smooth curve through the data, should be based upon an objective statistical treatment. It is important to realize that the placement of the continuum too low or too high will introduce *systematic errors* into measured quantities. These errors should be properly accounted for in the error budget. However, unlike statistical errors, which are derived from the variance spectrum and are uncorrelated from pixel to pixel, the error introduced into a given pixel by the continuum fit is correlated to the errors in nearby pixels. Using orthogonal functions for continuum modeling provide a straight forward and formally exact treatment of these correlated uncertainties.

The majority of a quasar SED is fairly flat and (in the absence of intervening absorbing gas) is quite featureless and smooth. As such, when the signal to noise ratio is high, it is not too challenging to estimate the continuum level over these regions. This can be done by fitting a low order polynomial (low frequency undulations) through the data. However, quasar SEDs can contain wavelength regions with complex features, especially BALs and highly peaked emission lines. These higher frequency features require higher order polynomials. Thus, in order to fit a complete spectrum, low order and higher order polynomials must be splined together. Performing a spline fit requires that the polynomial values and first derivative are equal at the spline knots, where the polynomials of different orders are tied together. It can be very difficult to implement a spline fit that provides a satisfactory estimate to the continuum at all wavelengths.

One way to circumvent this problem, is to model the continuum only over regions of the spectrum where scientific analysis is to be performed. Assuming a region of spectrum with wavelength range $\lambda_l \leq \lambda \leq \lambda_u$, where

λ_l and λ_u are the lower and upper wavelength extremes of the selected region, the central wavelength is

$$\bar{\lambda} = \frac{\lambda_u + \lambda_l}{2}. \quad (7.72)$$

A straight forward accounting of the uncertainties in the continuum, I_λ^c can be treated for a function that is the sum of $M + 1$ orthogonal functions, such as Legendre polynomials,

$$I_\lambda^c(x) = \sum_{k=0}^M a_k P_k(x), \quad (7.73)$$

where a_k are the coefficients (fitting parameters) for each polynomial of order k . The definition of P_k is

$$P_k(x) = \begin{cases} 1 & : k = 0 \\ x & : k = 1 \\ (3x^2 - 1)/2 & : k = 2 \\ [(2k - 1)xP_{k-1}(x) - (k - 1)P_{k-2}(x)]/k & : k \geq 3. \end{cases} \quad (7.74)$$

Legendre polynomials, as are all orthogonal polynomials, are symmetric (even order) or anti-symmetric (odd order) about $x = 0$ and, over the range $-1 \leq x \leq 1$, are orthonormal

$$\int_{-1}^1 P_j(x) P_k(x) dx = \begin{cases} 0 & : j \neq k \\ 1 & : j = k. \end{cases} \quad (7.75)$$

Orthogonal functions have coefficients that are independent for each order. In other words, with each successive higher order added in Eq. 7.73, the lower order coefficients are unchanged. To exploit the orthogonality, the independent variable must range from $-1 \leq x \leq 1$, which is obtained through the transform

$$x_i = \frac{\lambda_i - \bar{\lambda}}{\Lambda}, \quad (7.76)$$

where

$$\Lambda = \frac{\lambda_u - \lambda_l}{2} \quad (7.77)$$

is the normalization constant for the coordinate transformation. The coefficients can be determined using χ^2 minimization (§ 3.6), where

$$\chi_\nu = \sum_{i=1}^{N_{pix}} \frac{[I_\lambda(x_i) - P(x_i)]^2}{\sigma_{I_\lambda}^2(x_i)}, \quad (7.78)$$

is the reduced χ^2 , and $\sigma_{I_\lambda}(x_i)$ is the uncertainty in $I_\lambda(x_i)$. The degrees of freedom are $N_{pix} - (M + 1)$. The uncertainties in the coefficients are provided by the inverse of the curvature matrix (Eq. 3.118),

$$\sigma_{jk} = \alpha_{jk}^{-1} = C_{jk}, \quad (7.79)$$

where α_{ij} are the elements of the curvature matrix, and where C_{jk} are the elements of the inverse matrix, called the co-variance matrix. Without the property of orthogonality, all elements of the matrix would be correlated and the above simple expression would not be exactly true. The variance in the continuum, $\sigma_{I_\lambda^c}(x_i)$, is then determined at each x_i from

$$\sigma_{I_\lambda^c}^2(x_i) = \sum_{j=0}^M \sum_{k=0}^M \sigma_{a_{jk}}^2 P_j(x_i) P_k(x_i). \quad (7.80)$$

Thus, the errors in the fitted coefficients contain information about both the quality of the continuum fit (that it is not a representation of the true continuum) and, at each pixel i , the relative contribution of the accuracy of the continuum model due to each pixel included in the fit.

As an example of how the continuum error propagates into measurements, consider the flux decrement $D(x_i) = 1 - I_\lambda(x_i)/I_\lambda^c(x_i)$, at x_i . The variance is

$$\sigma_D^2(x_i) = \left(\frac{\partial D(x_i)}{\partial I_\lambda(x_i)} \right)^2 \sigma_{I_\lambda}^2(x_i) + \left(\frac{\partial D(x_i)}{\partial I_\lambda^c(x_i)} \right)^2 \sigma_{I_\lambda^c}^2(x_i) \quad (7.81)$$

where $\sigma_{I_\lambda}^2(x_i)$ is obtained directly from the variance spectrum, $\sigma_{I_\lambda^c}^2(x_i)$ is obtained from Eq. 7.80, and

$$\frac{\partial D(x_i)}{\partial I_\lambda(x_i)} = \frac{1}{I_\lambda^c(x_i)} \quad (7.82)$$

$$\frac{\partial D(x_i)}{\partial I_\lambda^c(x_i)} = -\frac{I_\lambda(x_i)}{[I_\lambda^c(x_i)]^2}, \quad (7.83)$$

giving

$$\sigma_D^2(x_i) = \left(\frac{\sigma_{I_\lambda}(x_i)}{I_\lambda^c(x_i)} \right)^2 + \left(\frac{I_\lambda(x_i) \sigma_{I_\lambda^c}(x_i)}{[I_\lambda^c(x_i)]^2} \right)^2, \quad (7.84)$$

where $I_\lambda^c(x_i)$ is given by Eq. 7.73, and the translation back to wavelength is given by Eqs. 7.76 and 7.77.

7.2.7 Combining Spectra

Often, in the case of long slit spectra, multiple observations have been obtained and must be combined into a single spectrum. In cases where echelle spectra have been obtained, it is desirable to combine the overlapping wavelength regions from adjacent orders. Combining the spectra requires a rebinning of the wavelength pixelization. This must be done with care. First, the flux must be conserved during the rebinning process. Second, the count level of each spectrum must in some fashion be on an equal scaling, either by flux calibration or normalization of the continuum.

The counts in the pixels of the original, or input spectra to the combining process, are not correlated. Each pixel is an independent measurement. However, the rebinning process will result in counts that are correlated in the output spectrum. Furthermore, if the pixel bin size of the output spectrum is fixed width, this linearizes the dispersion of the spectrum.

Consider a set of N_s spectra of the same object that have been acquired at different times. The process begins by accounting for the natural binning of the input spectra due to pixelization. In the j th spectrum, each pixel, i , has a central wavelength λ_{ji} , with width $\Delta\lambda_{ji}$, given by

$$\begin{aligned}\Delta\lambda_{ji} &= \lambda_{ji} - \lambda_{j,i-1} \\ \lambda_{ji}^- &= \lambda_{ji} - \frac{1}{2}\Delta\lambda_{ji} \\ \lambda_{ji}^+ &= \lambda_{ji} + \frac{1}{2}\Delta\lambda_{ji},\end{aligned}\tag{7.85}$$

where λ_{ji}^- and λ_{ji}^+ are the starting and ending wavelengths of the pixel (the pixel edges). Note that $\Delta\lambda_{ji}$ is not constant for all i because $\Delta\lambda \propto \lambda$. For the combined output spectrum, it is simplest to linearize the wavelength interval of the pixels. It is advantageous to set this interval to the maximum wavelength width of the input spectra (this avoids possible aliasing),

$$\Delta\lambda = \max(\Delta\lambda_{ji}),\tag{7.86}$$

where the lack of a subscript denotes the combined output spectrum pixelization. This combined output spectrum must cover the full range of the input spectra, so that

$$\begin{aligned}\lambda^{min} &= \min(\lambda_{ji}) \\ \lambda^{max} &= \max(\lambda_{ji}),\end{aligned}\tag{7.87}$$

where λ^{min} and λ^{max} are the beginning wavelength and ending wavelength of the combined output spectrum. The number of pixels in the output

spectrum is then

$$N = \frac{\lambda^{max} - \lambda^{min}}{\Delta\lambda}. \quad (7.88)$$

This information provides the wavelength pixelization of the output spectrum as follows,

$$\begin{aligned} \lambda_k &= \lambda^{min} + (k-1)\Delta\lambda & k = 1, N \\ \lambda_k^- &= \lambda_k - \frac{1}{2}\Delta\lambda \\ \lambda_k^+ &= \lambda_k + \frac{1}{2}\Delta\lambda, \end{aligned} \quad (7.89)$$

where λ_k is the wavelength center of pixel k , and λ_k^- and λ_k^+ are the starting and ending wavelengths of pixel k . The indexing is illustrated in Figure 7.14a. The pixelization of several input spectra, labeled j through $j+3$ (for $N_s = 4$) are shown, with details of the pixelization binning illustrated for pixel i of the j th spectrum (Eq. 7.85). The output spectrum binning is shown below input spectrum j , with the details of the pixelization shown for pixel k (Eqs. 7.86, 7.87, and 7.89).

To obtain the output spectrum requires a two step process. The first step is to resample the data for each input spectrum, j , to have the wavelength pixelization of the output spectrum. This process requires flux conservation, for interpolation of the flux values will be required since the pixels of each input spectrum will not necessarily align with the pixels of the output spectrum. This interpolation is based upon the fractional overlap of the input spectrum pixel and the output spectrum pixel. The flux conserving weights, w_{ji} , are

$$w_{ji} = \begin{cases} \frac{\lambda_{ji}^+ - \lambda_k^-}{\Delta\lambda_{ji}} & : \lambda_k^- < \lambda_{ji}^+ \leq \lambda_k^+ \\ & : \\ \frac{\lambda_k^+ - \lambda_{ji}^-}{\Delta\lambda_{ji}} & : \lambda_k^- < \lambda_{ji}^- \leq \lambda_k^+ \\ & : \\ 1 & : \text{both true} \\ & : \\ 0 & : \text{both false.} \end{cases} \quad (7.90)$$

The conditions account for the fraction of the counts in pixel i of spectrum j to be resampled into pixel k based upon a pixel area weighting scheme. As illustrated in upper portion of Figure 7.90b, the first condition of Eq. 7.90 provides the fraction of I_{ji} where the “red” region of pixel i of input spectrum j overlaps with pixel k . The center portion of Figure 7.90b

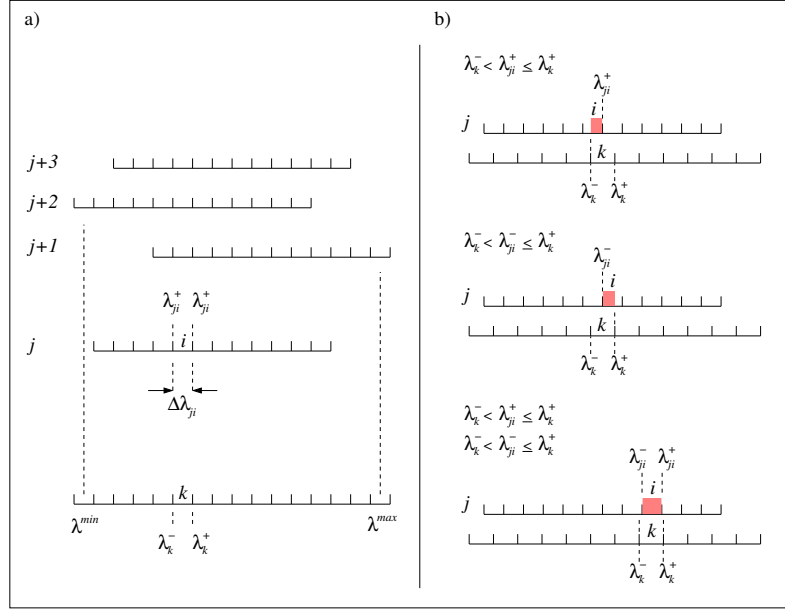


Figure 7.14: — (a) The pixelization of the input spectra are shown with details of the indexing for pixel i of spectrum j . The output spectrum is shown at the bottom of the panel. The minimum and maximum wavelengths are illustrated as is the book keeping indexing for pixel k . — (b) The rebinning of spectrum j onto the pixelization binning, k , of the output spectrum is illustrated for the three conditions of Eq. 7.90. The process accounts for fractional overlap of the pixels and conserves the flux in the rebinning process.

illustrates the second condition of Eq. 7.90 that provides the fraction of I_{ji} where the “blue” region of pixel i of input spectrum j overlaps with pixel k . The third condition of Eq. 7.90 applies when the pixel i of spectrum j aligns fully with pixel k , as is shown in the lower portion of Figure 7.90b. This latter condition is not common, but must be considered. The fourth condition (not illustrated) applies when there is no alignment between the input and output pixels for the given indices. A mask spectrum can also be created in which undesirable pixels can also have $w_{ji} = 0$. In the case of echelle spectra, additional book keeping can be introduced to account for the individual orders and their wavelength overlap.

If I_{ji} is the flux calibrated or the continuum normalized counts and σ_{ji} is the uncertainty in I_{ji} for pixel i in spectrum j , then the counts in

spectrum j resampled to pixel k is given by

$$I_{jk} = \frac{\sum_{i=1}^{N_j} w_{ji} I_{ji}}{\sum_{i=1}^{N_j} w_{ji}}, \quad (7.91)$$

and the uncertainty in I_{jk} is

$$\sigma_{jk} = \frac{\sum_{i=1}^{N_j} w_{ji} \sigma_{ji}}{\sum_{i=1}^{N_j} w_{ji}}, \quad (7.92)$$

where the sums are over the N_j pixels of spectrum j .

The second step, after all j spectra have been resampled to the output spectrum wavelength pixelization, is to compute the counts in pixel k from the optimally weighted mean of the N_s spectra,

$$I_k = \frac{\sum_{j=1}^{N_s} I_{jk} / \sigma_{jk}^2}{\sum_{j=1}^{N_s} 1 / \sigma_{jk}^2}, \quad (7.93)$$

where the sum is over all N_s spectra being combined. The variance in the I_k is given by

$$\sigma_k^2 = \left[\sum_{j=1}^{N_s} 1 / \sigma_{jk}^2 \right]^{-1}. \quad (7.94)$$

It is important to realize that the above treatment for combining individual spectra onto a common wavelength scale will have the undesirable effect of “smoothing” the flux values, which are now correlated. It is true that the signal-to-noise is improved as the number of combined spectra are increased, but the rebinning causes an additional and artificial enhancement to the noise characteristics. During subsequent analysis, this should be taken into account by including a small multiplicative factor for σ_k . This factor can be determined by comparing the variance in the spectrum in selected regions centered on pixel k to the value of σ_k^2 . This is a less than desirable, though commonly invoked, approach.

References

- Gray, D. F. 1992, *The Observational and Analysis of Stellar Photospheres*, (Cambridge University Press : Cambridge)
- Hecht, E. & Zajac, A. 1974, *Optics*, (Addison Wesley : Menlo Park)
- Horne, K. 1986, “An Optimal Extraction Algorithm for CCD Spectroscopy,” *PASP*, 98, 609
- Marsh, T. R. 1989, “The Extraction of Highly Distorted Spectra,” *PASP*, 101, 1032
- Schroeder, D. J. 1978, *Astronomical Optics*, (Academic Press : San Diego)